Topological edge states in the Su-Schrieffer-Heeger model

Daichi Obana,[1,*] Feng Liu,[1,†] and Katsunori Wakabayashi[1,2,‡]

[1]*Department of Nanotechnology for Sustainable Energy, School of Science and Technology, Kwansei Gakuin University, Gakuen 2-1, Sanda, Hyogo 669-1337, Japan*

[2]*National Institute for Materials Science, Tsukuba, Ibaraki 305-0044, Japan*

(Received 13 June 2019; published 29 August 2019)

The Su-Schrieffer-Heeger (SSH) model on a two-dimensional square lattice exhibits a topological phase transition which is related to the Zak phase determined by bulk band topology. The strong modulation of electron hopping causes nontrivial charge polarization even in the presence of inversion symmetry. The energy band structures and topological edge states have been calculated numerically in previous studies. Here, however, the full energy spectrum and explicit form of wave functions for two-dimensional bulk and one-dimensional ribbon geometries of the SSH model are analytically derived using the wave mechanics approach. Explicit analytic representations of wave functions provide the information of parity for each subband, localization length, and critical point of the topological phase transition in the SSH ribbon. IThe dimensional crossover of the topological transition point for the SSH model from one to two dimensions is also shown.

DOI: 10.1103/PhysRevB.100.075437

I. INTRODUCTION

The recent development of topological band theory in condensed-matter physics [1–3] has established a new class of electronic materials such as topological insulators [4–11], topological crystalline insulators [12–15], and topological semimetals [16–23]. In these topological materials, topologically protected edge states (TESs) emerge owing to nontrivial bulk band topology. TESs are robust to defects and edge roughness and can be exploited for application in low-power consumption electronic and spintronic devices. One origin of TESs is nonzero Berry curvature induced by spin-orbit couplings. Berry curvature is a geometric field strength in momentum space. Its integration over momentum space yields a magnetic monopole that is characterized by the Chern number.

Even under zero Berry curvature, the Berry connection, a geometric vector potential whose curl yields the Berry curvature, can also lead to TESs [24]. Integration of the Berry connection over momentum space (also called the Zak phase [25]) results in an electric dipole moment that generates robust fractional surface charges [26–28]. Such a dipole field related to the Zak phase is used to design topological materials, i.e., topological electrides [29,30] and A_3B atomic sheets such as C_3N [31,32]. Recently, this idea was extended to an electric quadrupole moment which induces topological corner states [33–40]. In addition, since topological design on the basis of the Zak phase does not demand the spin-orbit couplings, this approach is useful for application to nonelectronic systems such as topological photonics [41–45], acoustic crystals [46–49], and topological circuits [50,51].

One of the simplest models to demonstrate the topological phase transition owing to the Zak phase associated with zero Berry curvature is the Su-Schrieffer-Heeger (SSH) model [52,53] on a two-dimensional (2D) square lattice [24]. Essentially the same model was also introduced by Shockley to discuss the surface localized modes [54], which is nowadays known as Shockley model [55,56]. In these models, the topological phase transition occurs by tuning the ratio between inter- and intracell electron hoppings. If intercell hoppings become larger than the intracell hoppings, the Zak phase becomes nonzero, and edge states appear as a consequence of bulk-edge correspondence. However, the emergence of edge states in ribbon systems has been confirmed only by numerical calculations so far.

Meanwhile, graphene is another good example that provides the finite Zak phase accompanying TESs. Graphene has two characteristic edge structures, i.e., zigzag and armchair. Zigzag graphene edges provide the robust edge localized states at the Fermi energy [57–59], which can be attributed to the existence of the finite Zak phase in the bulk wave function of graphene [60–62]. Actually, edge states provide the perfectly conducting channel [63–65] and lead to very high conductivity in graphene nanoribbons [66]. However, armchair graphene edges do not provide such edge states at all owing to the zero Zak phase. Graphene nanoribbons are particularly advantageous since their complete energy spectrum and wave functions can be analytically obtained by solving the equations of motion of the tight-binding model using wave mechanics approaches [67,68].

In this paper, we analytically derive the full energy spectrum and corresponding wave functions of one-dimensional (1D) SSH ribbons using the wave mechanics approach. From the explicit form of the wave functions, we obtain the information of the parity for each subband, the localization length of the TES, and the critical point of the topological phase transition in 1D SSH ribbons to clarify the crossover from

*1227banao@kwansei.ac.jp
†ruserzzz@gmail.com
‡waka@kwansei.ac.jp

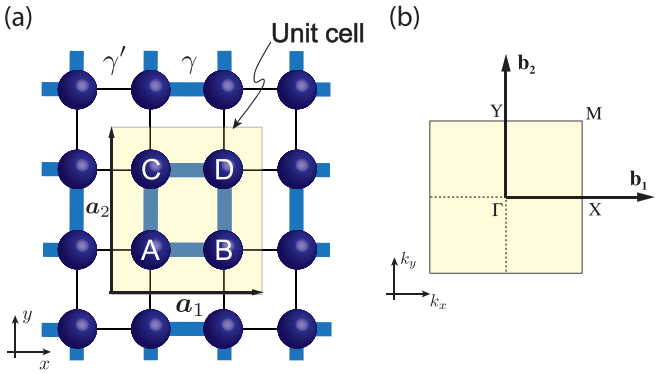

FIG. 1. (a) Schematic of the SSH model on a square lattice. Thick and thin bonds represent the intra- and intercell electron hoppings, respectively. The primitive translation vectors are $\boldsymbol{a_1} = (a, 0)$ and $\boldsymbol{a_2} = (0, a)$. (b) Corresponding first BZ. The reciprocal lattice vectors are $\boldsymbol{b_1} = (\frac{2\pi}{a}, 0)$ and $\boldsymbol{b_2} = (0, \frac{2\pi}{a})$.

the 1D to 2D system. In the 2D limit, the topological phase transition happens when the inter- and intracell hoppings are equal. However, in 1D SSH ribbons, it is found that stronger intercell hoppings are needed for the topological phase transition owing to the finite-size effect. It is also found that the critical value of the transition has a power-law dependence on the ribbon width.

This paper is organized as follows. In Sec. II, we give a brief summary of the energy spectrum and wave functions of the SSH model in the 2D limit, where the topological phase transition is related to the Zak phase. In Sec. III, we analytically derive the energy spectrum and corresponding wave functions of SSH ribbons by using the wave mechanics approach. The critical ratio between intra- and intercell electron hoppings for the topological phase transition is calculated by using the analytic solutions. Section IV provides a summary of the paper.

II. TWO-DIMENSIONAL SSH MODEL

In this section, we briefly discuss the electronic states and their topological properties in the 2D SSH model. Figure 1(a) shows a schematic of the 2D SSH model on a square lattice. The yellow shaded square indicates the unit cell, in which there are four atomic sites labeled A, B, C, and D. We assume that each atomic site possesses a single electron orbital and intra- and intercell hoppings, $-\gamma$ and $-\gamma'$, respectively. Here, γ and γ' are defined as positive real values. The primitive vectors are defined as $\boldsymbol{a_1} = (a, 0)$ and $\boldsymbol{a_2} = (0, a)$, where a is the lattice constant. The system has N_x cells along the x direction N_y cells along the y direction, resulting in a system size of $L_x = N_x a$ along the x direction and $L_y = N_y a$ along the y direction. Note that this system has a point group symmetry of C_{4v}. Since the system possesses both inversion and time-reversal symmetries, Berry curvature is absent in this system. Figure 1(b) shows the corresponding first Brillouin zone (BZ).

The eigenvalue equation of the 2D SSH model on a square lattice is written as

$$\hat{H}(\boldsymbol{k})|u_j(\boldsymbol{k})\rangle = \varepsilon_j(\boldsymbol{k})|u_j(\boldsymbol{k})\rangle, \tag{1}$$

TABLE I. Relation between band index j, eigenvalue ε_j, and eigenfunction u_j. ζ_j denotes the parity of the eigenvector at the M, X, and Γ points for the trivial (nontrivial) phase.

j	s_1	s_2	ε_j	u_j	$\zeta_j(M)$	$\zeta_j(X)$	$\zeta_j(\Gamma)$
1	−	−	ε_1	u_1	+ (+)	+ (−)	+ (+)
2	+	−	ε_2	u_2	− (−)	− (+)	− (−)
3	−	+	ε_3	u_3	− (−)	− (+)	− (−)
4	+	+	ε_4	u_4	+ (+)	+ (−)	+ (+)

where $\boldsymbol{k} = (k_x, k_y)$ is the wave number vector and j $(= 1, 2, 3, 4)$ is the band index. The eigenvector is defined as $|u_j(\boldsymbol{k})\rangle = (\psi_{j,A}(\boldsymbol{k}), \psi_{j,B}(\boldsymbol{k}), \psi_{j,C}(\boldsymbol{k}), \psi_{j,D}(\boldsymbol{k}))^T$, where $(\cdots)^T$ indicates the transpose of the vector. $\psi_{j,\alpha}(\boldsymbol{k})$ $(\alpha = A, B, C, D)$ is the amplitude at site α for the jth energy band at $\boldsymbol{k}$. The Hamiltonian $\hat{H}(\boldsymbol{k})$ is explicitly written as

$$\hat{H}(\boldsymbol{k}) = \begin{pmatrix} 0 & -\rho_x(k_x) & -\rho_y(k_y) & 0 \\ -\rho_x^*(k_x) & 0 & 0 & -\rho_y(k_y) \\ -\rho_y^*(k_y) & 0 & 0 & -\rho_x(k_x) \\ 0 & -\rho_y^*(k_y) & -\rho_x^*(k_x) & 0 \end{pmatrix}, \tag{2}$$

where $\rho_l(k_l) = \gamma + \gamma' e^{ik_l a} = |\rho_l(k_l)|e^{i\phi_l(k_l)}$, with $l = x, y$. Here, $\phi_l(k_l)$ is defined as the argument of $\rho_l(k_l)$ with a range of $-\pi \leqslant \phi_l(k_l) \leqslant \pi$.

By solving Eq. (1), the energy spectra for bulk states are obtained as

$$\varepsilon_j(\boldsymbol{k}) = s_1|\rho_x(k_x)| + s_2|\rho_y(k_y)|, \tag{3}$$

where $s_1 = s_2 = \pm 1$. The energy spectrum contains four subbands; the relations between the band index j and signs s_1 and s_2 are summarized in Table I. Eigenvectors for bulk states are obtained as

$$|u_j(\boldsymbol{k})\rangle = \frac{1}{2}\begin{pmatrix} -1 \\ s_1 e^{-i\phi_x(k_x)} \\ s_2 e^{-i\phi_y(k_y)} \\ -s_1 s_2 e^{-i[\phi_x(k_x)+\phi_y(k_y)]} \end{pmatrix}. \tag{4}$$

Figures 2(a) and 2(b) show the energy band structures for $\gamma'/\gamma \neq 1$ and $\gamma'/\gamma = 1$, respectively. In general, the energy band structures of the 2D SSH model become identical

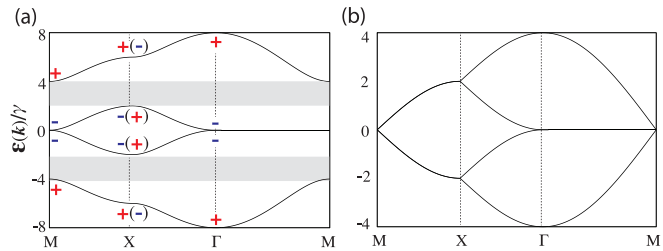

FIG. 2. Energy band structure of the 2D SSH model for (a) $\gamma'/\gamma = 1/3.0$ $(\gamma'/\gamma = 3.0)$ and (b) $\gamma'/\gamma = 1$. The signs $(\pm)$ in the plot of the energy band structure represent the parity of the wave function. It should be noted that band inversion occurs at the $X(Y)$ point.

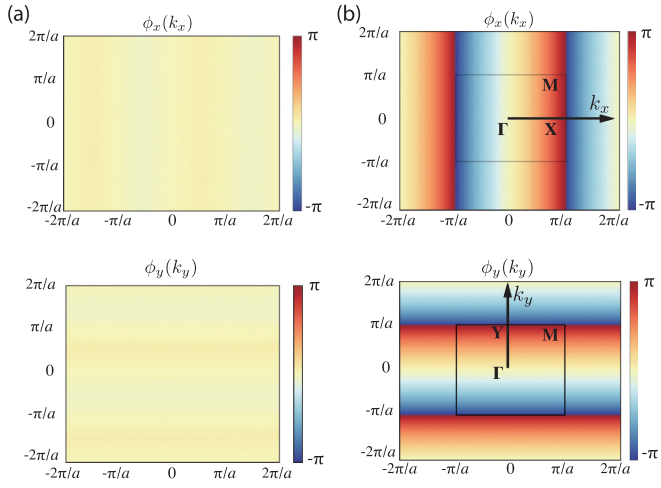

FIG. 3. Density plot of the phase $\phi_l(k_l)$ for (a) trivial and (b) nontrivial phases. In the trivial phase, no phase jumps occurs. In the nontrivial phase, however, the phase jumps by 2π occur along the lines of $k_x = \pm\pi$ and $k_y = \pm\pi$, respectively.

between cases with the ratio γ'/γ and its inverse ratio γ/γ'. For finite γ'/γ, two band gaps open between the first and second subbands and between the third and fourth subbands. The band gaps close at $\gamma'/\gamma = 1$. However, it should be noted that the parities at the $X(Y)$ point are inverted between the regions of $\gamma'/\gamma \leqslant 1$ and $\gamma'/\gamma > 1$.

The topological properties of the 2D SSH model can be characterized in terms of the vectored Zak phase $\boldsymbol{\mathcal{Z}} = (\mathcal{Z}_x, \mathcal{Z}_y)$, which is defined as the line integration of the Berry connection. The Berry connection for the jth energy band is defined as $\boldsymbol{A}_j = (a_j(k_x), a_j(k_y))$, with $a_j(k_l) = -i\langle u_j(\boldsymbol{k})|\frac{\partial}{\partial k_l}|u_j(\boldsymbol{k})\rangle$. Since the band inversion happens in the 2D SSH model at $\gamma'/\gamma = 1$, the finite Zak phase appears for $|\gamma'/\gamma| > 1$ and is absent for $|\gamma'/\gamma| \leqslant 1$. In the case of the finite Zak phase, the system possesses charge polarization, which induces the TESs. From now on, we call the phase with the finite Zak phase the *nontrivial* phase; otherwise, we have the *trivial* phase. The lth component of the vectored Zak phase in the 2D SSH model can be related to the winding phase of the eigenvectors as

$$\begin{aligned}\mathcal{Z}_l &= -i\sum_{j=1}^{occ.}\int_0^{2\pi}\langle u_j(\boldsymbol{k})|\frac{\partial}{\partial k_l}|u_j(\boldsymbol{k})\rangle\, dk_l \\ &= N_{occ.}\frac{1}{2}\Delta\phi_l(k_l),\end{aligned} \tag{5}$$

where $\Delta\phi_l(k_l)$ is the winding phase of the eigenvectors accompanied by the variation of k_l from zero to 2π and $N_{occ.}$ is the number of occupied energy bands. The derivation of Eq. (5) is given in Appendix A.

Figures 3(a) and 3(b) show the density plot of phase ϕ_l in the trivial and nontrivial phases, respectively. In the trivial case, the magnitude of the phase is almost zero everywhere in momentum space. However, in the nontrivial case, phases ϕ_x and ϕ_y jump by 2π along the lines of $k_x = \pm\pi$ and $k_y = \pm\pi$, respectively. By looking at these figures, we can find the Zak phase as follows:

$$\mathcal{Z}_l = \frac{1}{2}\Delta\phi_l(k_l) = \begin{cases}0 & \gamma'/\gamma \leqslant 1, \\ \pi & \gamma'/\gamma > 1.\end{cases} \tag{6}$$

Thus, the nontrivial phase appears for $\gamma'/\gamma > 1$. The derivation of Eq. (6) is given in Appendix A.

Zak phases are related to charge polarization $\boldsymbol{P} = (P_x, P_y)$ as follows [26,27]:

$$P_l = -i\frac{1}{L_l}\sum_{j=1}^{occ.}\sum_{k_l=-\pi}^{\pi}\langle u_j(\boldsymbol{k})|\frac{\partial}{\partial k_l}|u_j(\boldsymbol{k})\rangle = \frac{\mathcal{Z}_l}{2\pi}. \tag{7}$$

Thus, if the system has the nonzero Zak phase, charge polarization occurs, i.e., the appearance of edge states. Because of C_4 symmetry, the 2D SSH model has $P_x = P_y$ in general. Thus, charge polarization of the 2D SSH model is $\boldsymbol{P} = (0, 0)$ for the trivial phase and $(1/2, 1/2)$ for the nontrivial phase.

Inversion symmetry puts a strong constraint on the value of $\boldsymbol{P}$, which is determined gauge independently by the parities at the Γ and X (Y) points as [69]

$$P_l^j = \tfrac{1}{2}\left(q_l^j \bmod 2\right), \tag{8}$$

$$(-1)^{q_x^j} = \prod_{j\in occ.}\frac{\zeta_j(\mathrm{X})}{\zeta_j(\Gamma)}, \quad (-1)^{q_y^j} = \prod_{j\in occ.}\frac{\zeta_j(\mathrm{Y})}{\zeta_j(\Gamma)}, \tag{9}$$

where P_l^j indicates the lth charge polarization and q_l^j is topologically invariant, which is 0 or 1. The details of Eq. (8) and (9) are described in Appendix B. Thus, the value of the Zak phase determines the presence or absence of electrical polarization.

Since the present system has a point group symmetry of C_{4v}, it has mirror symmetry M_x (M_y) with respect to the x (y) axis. In our system, M_x and M_y commute. However, the inclusion of π flux in the system makes M_x and M_y noncommutative, which leads to a gap opening in the Wannier band and topological quadrupole corner states [33].

III. EIGENSYSTEM OF SSH RIBBONS

In this section, we analytically derive the energy spectrum and corresponding wave functions of 1D SSH ribbons by using the wave mechanics approach under the open boundary condition. This method has been successfully used to derive the energy spectrum and wave functions for graphene nanoribbons to show the existence of edge states [67,68]. Explicit wave functions provide information of the parity for each subband and the localization length of the TES. We also inspect the topological properties of a 1D SSH ribbon and the crossover from a one-dimensional to 2D system. In the 2D limit, the topological phase transition happens when the inter- and intracell hoppings are equal. However, in the 1D SSH ribbon, it is found that stronger intercell hoppings are needed for the topological phase transition owing to the finite-size effect. It is also found that the critical value of the transition has a power-law dependence on the ribbon width. We also show the localization length of the TES for 1D SSH ribbons strongly depends on γ'/γ.

Figure 4 shows the schematic structure of a SSH ribbon, where we assume that the lattice is translationally invariant

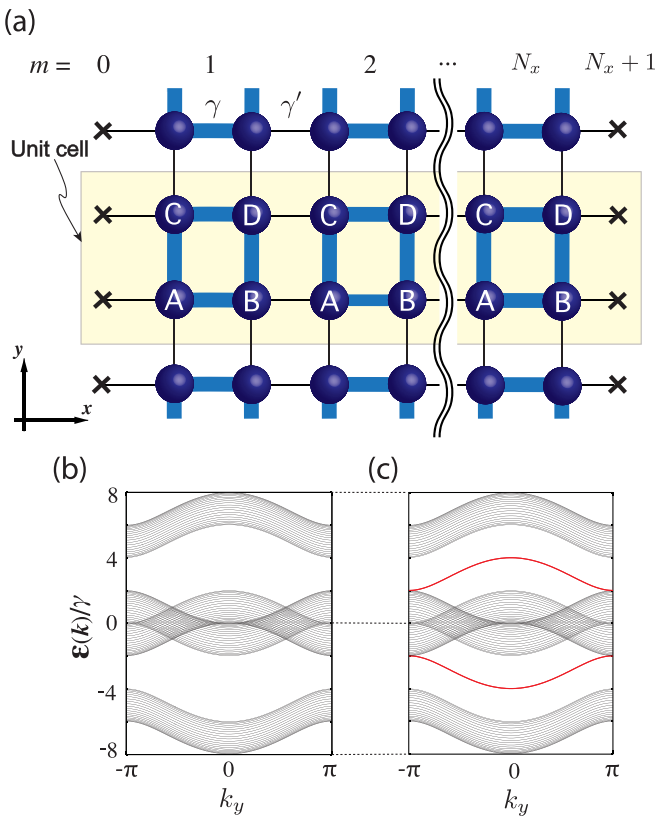

FIG. 4. (a) SSH ribbon model on a square lattice. N_x is the ribbon width. The × marks indicate the missing atoms for the open boundary condition. Energy band structure of $N_x = 20$ for (b) $\gamma'/\gamma = 1/3.0$ and (c) $\gamma'/\gamma = 3.0$. In the nontrivial case, edge states appear (red lines).

only along the y direction and is finite for the x direction. From now on, we assume $a = 1$ for simplicity. The yellow shaded rectangle indicates the unit cell of the SSH ribbon, which contains N_x plaquettes, i.e., $4 \times N_x$ atomic orbitals. We call the four atomic sites of the mth plaquette mA, mB, mC, and mD and define the corresponding wave functions as $\psi_{m,A}$, $\psi_{m,B}$, $\psi_{m,C}$, and $\psi_{m,D}$, where $m = 0, 1, \ldots, N_x + 1$.

The equations of motion for a 1D SSH ribbon are described by

$$\begin{aligned}
\varepsilon\psi_{m,A} &= -\rho_y^*\psi_{m,C} - \gamma\psi_{m,B} - \gamma'\psi_{m-1,B},\\
\varepsilon\psi_{m,B} &= -\rho_y^*\psi_{m,D} - \gamma\psi_{m,A} - \gamma'\psi_{m+1,A},\\
\varepsilon\psi_{m,C} &= -\rho_y\psi_{m,A} - \gamma\psi_{m,D} - \gamma'\psi_{m-1,D},\\
\varepsilon\psi_{m,D} &= -\rho_y\psi_{m,B} - \gamma\psi_{m,C} - \gamma'\psi_{m+1,C}.
\end{aligned} \tag{10}$$

The open boundary conditions for a 1D SSH ribbon are given as

$$\psi_{0,B} = \psi_{0,D} = 0, \quad \psi_{N_x+1,A} = \psi_{N_x+1,C} = 0. \tag{11}$$

Before explaining the analytic details, we shall briefly discuss the energy band structures of the ribbon. Figures 4(b) and 4(c) show energy band structures with $N_x = 20$ in the trivial phase with $\gamma'/\gamma = 1/3.0 \leqslant 1$ and the nontrivial phase with $\gamma'/\gamma = 3.0 > 1$, respectively. These band structures were numerically obtained by solving the equations of motion. In the trivial phase, gapped energy band structures are obtained. However, in the nontrivial phase, doubly degenerate TESs appear inside the gaps (indicated by magenta lines).

Now let us derive the eigensystem of 1D SSH ribbons by assuming the generic solutions of wave functions as

$$\psi_{m,\sigma} = C_\sigma e^{ik_x m} + \tilde{C}_\sigma e^{-ik_x m}, \tag{12}$$

where $\sigma = A, B, C, D$. C_σ and $\tilde{C}_\sigma$ are arbitrary coefficients. The open boundary condition leads to the following relations:

$$\begin{aligned}
\psi_{N_x+1,A} &= C_A Z + \tilde{C}_A Z^{-1} = 0,\\
\psi_{N_x+1,C} &= C_C Z + \tilde{C}_C Z^{-1} = 0,\\
\psi_{0,B} &= C_B + \tilde{C}_B = 0,\\
\psi_{0,D} &= C_D + \tilde{C}_D = 0,
\end{aligned} \tag{13}$$

where $Z = e^{ik_x(N_x+1)}$. Thus, we can rewrite the generic solution as

$$\begin{aligned}
\psi_{m,A} &= C_A(e^{ik_x m} - Z^2 e^{-ik_x m}),\\
\psi_{m,B} &= C_B(e^{ik_x m} - e^{-ik_x m}),\\
\psi_{m,C} &= C_C(e^{ik_x m} - Z^2 e^{-ik_x m}),\\
\psi_{m,D} &= C_D(e^{ik_x m} - e^{-ik_x m}).
\end{aligned} \tag{14}$$

By substituting these functions into the equations of motion, we obtain the secular equation for the 1D SSH ribbon,

$$\hat{\boldsymbol{M}}\Psi = 0, \tag{15}$$

where $\Psi = (C_A, C_B, C_C, C_D)^T$ and $\hat{\boldsymbol{M}}$ is a 4×4 matrix. The matrix elements $M_{i,j}$ $(i, j = 1, 2, 3, 4)$ of $\hat{\boldsymbol{M}}$ are

$$\begin{aligned}
M_{11} &= M_{33} = \varepsilon(e^{ik_x m} - e^{-ik_x m}Z^2),\\
M_{22} &= M_{44} = \varepsilon(e^{ik_x m} - e^{-ik_x m}),\\
M_{21} &= M_{43} = \rho_x e^{ik_x m} - \rho_x^* e^{-ik_x m}Z^2,\\
M_{12} &= M_{34} = \rho_x^* e^{ik_x m} - \rho_x e^{-ik_x m},\\
M_{13} &= \rho_y^*(e^{ik_x m} - e^{-ik_x m}Z^2),\\
M_{24} &= \rho_y^*(e^{ik_x m} - e^{-ik_x m}),\\
M_{31} &= \rho_y(e^{ik_x m} - e^{-ik_x m}Z^2),\\
M_{42} &= \rho_y(e^{ik_x m} - e^{-ik_x m}),\\
M_{14} &= M_{23} = M_{32} = M_{41} = 0.
\end{aligned} \tag{16}$$

It should be noted that $\Psi = 0$ and $k_x = 0, \pm\pi$ are unphysical solutions because wave functions $\psi_{m,\sigma}$ become identically zero; that is, electrons are absent in the system. Thus, $\det\hat{\boldsymbol{M}} = 0$ is demanded and leads to the following form:

$$ue^{4ik_x m} + ve^{2ik_x m} + w + ve^{-2ik_x m}Z^2 + ue^{-4ik_x m}Z^4 = 0, \tag{17}$$

where u, v, and w are functions of ε, ρ_y, γ, γ', and Z. Thus, all the coefficients of the $e^{\pm i4k_x m}$, $e^{\pm i2k_x m}$ terms and the constant term should be zero to hold Eq. (15), i.e., $u = 0$, $v = 0$, and $w = 0$.

By using space-inversion symmetry, i.e., $\psi_{N_x+1-m,A} = \pm\psi_{m,D}$, $\psi_{N_x+1-m,C} = \pm\psi_{m,B}$, we can obtain the relations $C_D = \pm C_A Z$ and $C_B = \pm C_C Z$ from Eq. (14). In addition, the mirror symmetry leads to $\psi_{m,A} = \pm\psi_{m,C}$, i.e., $C_C = \pm C_A$. Thus, the general form of the wave function can be written

as

$$\begin{pmatrix}\psi_{m,A}\\ \psi_{m,B}\\ \psi_{m,C}\\ \psi_{m,D}\end{pmatrix} = N_c \begin{pmatrix}\sin[k_x(N_x+1-m)]\\ (-1)^r s_1 \sin[k_x m]\\ s_2 \sin[k_x(N_x+1-m)]\\ (-1)^r s_1 s_2 \sin[k_x m]\end{pmatrix}, \tag{18}$$

where $r = 1, 2, 3, \ldots, N_x$ indicates the band index of the 1D SSH ribbon. However, as will be clarified later, the index will be $r = 1, 2, 3, \ldots, N_x - 1$ in the nontrivial phase because the one missing mode will form the mode of TESs. It should be noted that the parity of the wave function clearly depends on the band index r. N_c is the normalization constant. Owing to the translational invariance along the y direction, the wave function for the whole ribbon system can be obtained by multiplying the Bloch phase $e^{ik_y y}$ and Eq. (18).

The coefficients of $e^{\pm i4k_x m}$ are shown to be identically zero by using the bulk energy spectrum equation (3), i.e.,

$$\begin{aligned} u(k_x, k_y, N_x) &= \varepsilon^4 - 2\varepsilon^2(|\rho_x|^2 + |\rho_y|^2)^2 + (|\rho_x|^2 - |\rho_y|^2)^2 \\ &= \{\varepsilon^2 - (|\rho_x| \pm |\rho_y|)^2\}^2 = 0. \end{aligned} \tag{19}$$

Thus, $u(k_x, k_y, N_x)$ is irrelevant for later discussion.

The solutions of $v = w = 0$ determine the transverse wave number k_x for a given γ'/γ. Thus, we obtain

$$\begin{aligned} v(k_x, k_y, N_x) = {} & \varepsilon^4[Z + Z^{-1}] - \varepsilon^2\big[\big(\rho_x^{*2} + |\rho_x|^2 + 2|\rho_y|^2\big)Z \\ & + \big(\rho_x^2 + |\rho_x|^2 + 2|\rho_y|^2\big)Z^{-1}\big] \\ & + (|\rho_x|^2 - |\rho_y|^2)\big[\big(\rho_x^{*2} - |\rho_y|^2\big)Z \\ & + \big(\rho_x^2 - |\rho_y|^2\big)Z^{-1}\big] = 0, \end{aligned} \tag{20}$$

$$\begin{aligned} w(k_x, k_y, N_x) = {} & \varepsilon^4[Z^2 + Z^{-2} + 4] - 2\varepsilon^2\big[\big(\rho_x^{*2} + |\rho_y|^2\big)Z^2 \\ & + \big(\rho_x^2 + |\rho_y|^2\big)Z^{-2} + \big(\rho_x + \rho_x^*\big)^2 + 4|\rho_y|^2\big] \\ & + \big(\rho_x^{*2} - |\rho_y|^2\big)^2 Z^2 + \big(\rho_x^2 - |\rho_y|^2\big)^2 Z^{-2} \\ & + 4\rho_x^2\rho_x^{*2} - 2|\rho_y|^2(\rho_x + \rho_x^*)^2 + 4|\rho_y|^4 = 0. \end{aligned} \tag{21}$$

It should be noted that both $v(k_x, k_y, N_x)$ and $w(k_x, k_y, N_x)$ are periodic and even functions of k_x with a period of 2π, i.e., $v(k_x, k_y, N_x) = v(-k_x, k_y, N_x)$ and $v(k_x + 2n\pi, k_y, N_x) = v(k_x, k_y, N_x)$ (n is an arbitrary integer). Similarly, $w(k_x, k_y, N_x)$ has the properties of $w(k_x, k_y, N_x) = w(-k_x, k_y, N_x)$ and $w(k_x + 2n\pi, k_y, N_x) = w(k_x, k_y, N_x)$. Thus, it is sufficient to find the solutions within the range $0 < k_x < \pi$.

At $\gamma'/\gamma = 1$, Eqs. (20) and (21) safely reproduce the energy spectrum of a simple 2D square lattice, i.e., $\varepsilon(\boldsymbol{k}) = \pm 2\gamma[\cos(\frac{k_x}{2}) \pm \cos(\frac{k_y}{2})]$. In addition, the open boundary condition for the ribbon structure leads to the transverse wave numbers k_x as

$$k_x = \frac{m}{N_x + 1}\pi, \quad m = 1, 2, 3, \ldots, N_x. \tag{22}$$

Figures 5(a) and 5(b) show the k_x dependence of $u(k_x, k_y, N_x)$, $v(k_x, k_y, N_x)$, and $w(k_x, k_y, N_x)$ for trivial and nontrivial phases, respectively. Here, we have fixed the ribbon width as $N_x = 5$. The functions $u(k_x, k_y, N_x)$, $v(k_x, k_y, N_x)$, and $w(k_x, k_y, N_x)$ are calculated under the condition $\varepsilon^2 = (|\rho_x| + |\rho_y|)^2$. The case of $\varepsilon^2 = (|\rho_x| - |\rho_y|)^2$ is not shown because the results do not change. The solutions of $u(k_x, k_y, N_x)$, $v(k_x, k_y, N_x)$, and $w(k_x, k_y, N_x)$, which are denoted by black circles in Figs. 5(a) and 5(b), give the transverse wave numbers k_x which determine the eigenstates of the 1D SSH ribbon. The variation of the longitudinal wave number k_y alters only the amplitude of $u(k_x, k_y, N_x)$, $v(k_x, k_y, N_x)$, and $w(k_x, k_y, N_x)$ and does not change the positions of the zero points. Thus, the solutions of $\det\boldsymbol{M} = 0$ do not depend on k_y.

For a fixed N_x, the number of real solutions N for $\det\hat{\boldsymbol{M}} = 0$ becomes different depending on the value of γ'/γ, i.e.,

$$N = \begin{cases} N_x, & |\gamma'/\gamma| \leqslant (\gamma'/\gamma)_c, \\ N_x - 1, & |\gamma'/\gamma| > (\gamma'/\gamma)_c. \end{cases} \tag{23}$$

Here, $(\gamma'/\gamma)_c$ is the critical value at which the topological phase transition occurs. $(\gamma'/\gamma)_c$ can be derived by

$$\frac{\partial}{\partial k_x} v(k_x, k_y, N_x)|_{k_x=\pi} = 0. \tag{24}$$

Further, as indicated by Eq. (23), one real solution is missing for $|\gamma'/\gamma| > (\gamma'/\gamma)_c$. This disappearance of a real solution happens near $k_x = \pi$ by looking at $w(k_x, k_y, N_x)$ under the evolution of γ'/γ, as shown in the insets of Figs. 5(a) and 5(b). Thus, the remaining missing solution can be obtained by analytical continuation of $k_x \to \pi + i\eta$. This imaginary solution η depends on γ'/γ. If γ'/γ is larger, η also increases.

Figures 5(c) and 5(d) show the relation between the obtained transverse complex wave number $(k_x + i\eta)$ and energy band structures of 1D SSH ribbons with $N_x = 5$ for trivial and nontrivial phases, respectively. In the trivial phase, as shown in Fig. 5(c), no imaginary solutions appear. The real transverse wave numbers k_x (denoted by thick black lines) lead to the energy subbands of extended bulk states. However, in the trivial phase, as shown in Fig. 5(d), an imaginary solution η appears, which gives the subband of TESs (thin magenta lines). Note that edge states are doubly degenerate owing to inversion symmetry.

The wave function of TESs can be written as

$$\begin{pmatrix}\psi_{m,A}\\ \psi_{m,B}\\ \psi_{m,C}\\ \psi_{m,D}\end{pmatrix} = N_c \begin{pmatrix}\sinh[\eta(N_x+1-m)]\\ (-1)^{N_x} s_1 \sinh[\eta m]\\ s_2 \sinh[\eta(N_x+1-m)]\\ (-1)^{N_x} s_1 s_2 \sinh[\eta m]\end{pmatrix}, \tag{25}$$

where N_c is the normalization constant. Similar to the extended states, the wave function of TESs for the whole ribbon system can be obtained by multiplying the Bloch phase $e^{ik_y y}$ and Eq. (25). It should be noted that the parity of TESs depends on N_x, resulting in the even-odd effect of N_x on the parity. This property can be used for a band-selective filter [70]. We should note that the wave function for TESs contains hyperbolic sine functions which are characterized by the imaginary transverse wave number η. Thus, TESs are localized states with a characteristic localization length of $1/\eta$.

Figure 6(a) shows the electron hopping (γ'/γ) dependence of the localization length $(1/\eta)$. Here, $1/\eta$ decays with the power law on increasing γ'/γ. With an increase of γ'/γ, the localization length of TESs becomes shorter; that is, electrons are more strongly localized near the edges of ribbon. Thus,

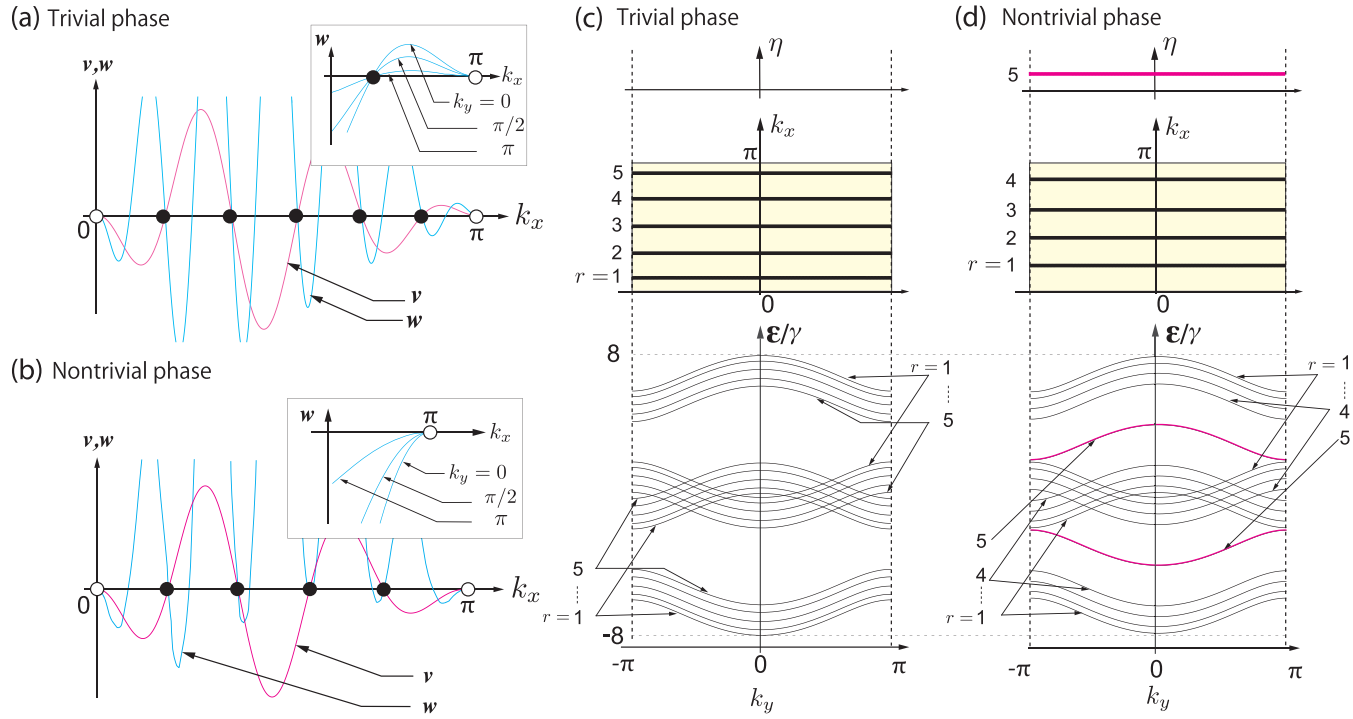

FIG. 5. Schematic chart of functions v (magenta line) and w (cyan line) for $N_x = 5$ in (a) the trivial $[|\gamma'/\gamma| \leqslant (\gamma'/\gamma)_c]$ and (b) nontrivial $[|\gamma'/\gamma| > (\gamma'/\gamma)_c]$ phases, respectively. White circles at $k_x = 0$ and π are unphysical solutions. The black circle in the region of $0 < k_x < \pi$ indicates the real-value solution of the transverse wave number k_x. It should be noted that there are N_x solutions for the trivial phase but only $N_x - 1$ solutions for the nontrivial phase. The insets show the dependence of w on the longitudinal wave number k_y near $k_x = \pi$. The relation between the obtained complex transverse wave number $k_x + i\eta$ and the corresponding energy band structure for the 1D SSH model with $N_x = 5$ for (c) the trivial and (d) nontrivial phases. In the top panels of (c) and (d), solutions of the complex transverse wave number $k_x + i\eta$ in the BZ are plotted. Both k_x and η do not have k_y dependence, and no imaginary part exists in the trivial phase. The bottom panels of (c) and (d) show the corresponding energy band structures. Real-value solutions k_x lead to energy dispersion of bulk states, denoted by thin black lines; however, the imaginary solution η leads to energy dispersion of TESs, denoted by thin magenta lines.

if the localization length is larger than the ribbon width, the destructive interference between TESs from both edges occurs. Actually, this property of TESs demands that stronger γ'/γ is necessary to induce the topological phase transition if the ribbon width gets narrower. Figure 6(b) shows the ribbon width N_x dependence of $(\gamma'/\gamma)_c$, which is the critical value for the topological phase transition. Although $(\gamma'/\gamma)_c = 1$ for a 2D SSH model, Figure 6(b) shows that narrower SSH ribbons have $(\gamma'/\gamma)_c$ larger than 1. Since $(\gamma'/\gamma)_c$ slowly decays with increasingN_x owing to its power-law behavior, the finite-size effect persists even for very large N_x. Thus, the finite-size effect for the topological phase transition in the 1D SSH model becomes crucial, especially for narrower ribbons.

IV. SUMMARY

In summary, we have analytically derived eigensystems of 2D SSH and 1D SSH ribbon models on a square lattice by using the wave mechanics approach. In these models, the modulation of electron hopping causes nontrivial charge polarization even in the presence of inversion symmetry. As for the 2D SSH model, it is known that the topological phase transition occurs, accompanied by nontrivial charge polarization if intercell hopping γ' is larger than intracell hopping γ. Owing to the bulk-edge correspondence, TESs are expected to appear in the nontrivial phase. However, this has been confirmed only by numerical calculations so far. In this paper, we have successfully derived the full energy spectrum and corresponding wave functions for 1D SSH ribbons by using the wave mechanics approach. Mathematical relations between the complex transverse wave number $(k_x + i\eta)$ and energy band structures of the 1D SSH ribbon were clarified. Also, the parity of wave functions and localization length of TESs were analytically identified.

It was also found that the critical value of the topological phase transition $(\gamma'/\gamma)_c$ strongly depends on the ribbon width and deviates from 1, which is the limit of the 2D SSH model. This information will be necessary when we try to fabricate topological electronic, photonic devices in quasi-1D geometry on the basis of the SSH model.

By using the wave function used in this paper, we can discuss further electronic states of the 2D SSH model subjected to other perturbations. Our approach is useful for constructing of Green's functions by the decomposition of propagating and evanescent modes, which is needed for atomistic calculations of electronic transport properties [71]. It is also possible to apply our approach to obtain the bound states of a finite 1D SSH model [72]. Our results will serve to design 2D materials which possess a nonzero Zak phase and edge states which are necessary for robust electronic transport. Furthermore, it can be applied to the theory of topological photonic crystals.

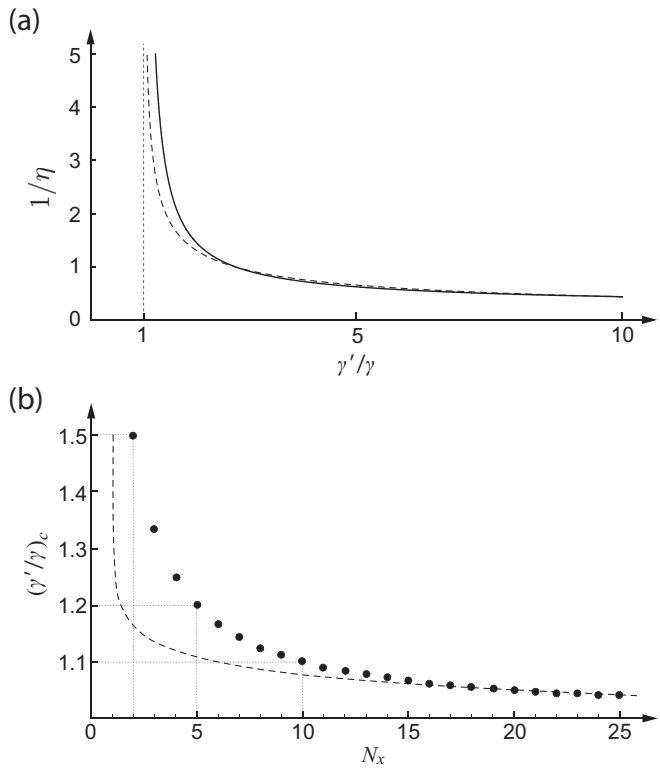

FIG. 6. (a) Dependence of the localization length $1/\eta$ of TES on γ'/γ. The solid line is calculated from analytic wave functions of Eq. (25). The dashed line is the fitting for the large coupling limit. The fitting curve is $1/\eta = 1.327(\gamma'/\gamma - 1)^{-0.481}$. (b) Ribbon width N_x dependence of the critical value $(\gamma'/\gamma)_c$, where the topological phase transition occurs. In the 2D limit of $N_x \to \infty$, $(\gamma'/\gamma)_c$ converges to 1. Black circles are $(\gamma'/\gamma)_c$ obtained from Eq. (24). The dashed line is the fitting for the limit of large N_x. The fitting curve is $(\gamma'/\gamma)_c = 1.165(N_x - 1)^{-0.034}$.

ACKNOWLEDGMENTS

F.L. is supported by the Postdoctoral Fellowship of the Japan Society for the Promotion of Science (JSPS). K.W. acknowledges the financial support from the Masuya Memorial Research Foundation of Fundamental Research. This work was supported by JSPS KAKENHI Grants No. JP17F17326 and No. JP18H01154.

APPENDIX A: DERIVATION OF EQUATIONS (5) AND (6)

Here, we derive the relation between the Zak phase and the winding phase of the eigenvectors given in Eqs. (5) and (6). From the eigenvector in Eq. (4), we obtain

$$\langle u_j(\boldsymbol{k})|\frac{\partial}{\partial k_l}|u_j(\boldsymbol{k})\rangle = \frac{i}{2}\frac{d\phi_l(k_l)}{dk_l}. \tag{A1}$$

Thus, Eq. (5) can be derived as

$$\begin{aligned}\mathcal{Z}_l &= -i\sum_{j=1}^{occ.}\int_0^{2\pi}\langle u_j(\boldsymbol{k})|\frac{\partial}{\partial k_l}|u_j(\boldsymbol{k})\rangle\, dk_l \\ &= N_{occ.}\frac{1}{2}\int_0^{2\pi} dk_l \frac{d\phi_l(k_l)}{dk_l} \\ &= N_{occ.}\frac{1}{2}\oint d\phi_l(k_l) \\ &=: N_{occ.}\frac{1}{2}\Delta\phi_l(k_l),\end{aligned} \tag{A2}$$

where $\Delta\phi_l(k_l)$ is the winding phase of the eigenvectors accompanied by the variation of k_l from zero to 2π and $N_{occ.}$ is the number of occupied energy bands.

From $\rho_l(k_l) = |\rho_l(k_l)|e^{i\phi_l(k_l)}$, the total derivative of $\rho_l(k_l)$ is obtained as

$$d\rho_l(k_l) = e^{i\phi_l(k_l)}d|\rho_l(k_l)| + i|\rho_l(k_l)|e^{i\phi_l(k_l)}d\phi_l(k_l). \tag{A3}$$

Identically, we have

$$\frac{1}{\rho_l(k_l)}d\rho_l(k_l) = \frac{1}{|\rho_l(k_l)|}d|\rho_l(k_l)| + id\phi_l(k_l). \tag{A4}$$

By taking the contour integration for both sides, we obtain the winding phase of the eigenvectors as

$$\frac{1}{i}\oint\frac{1}{\rho_l(k_l)}d\rho_l(k_l) = \Delta\phi_l(k_l), \tag{A5}$$

where $\rho_l(k_l) = \gamma'/\gamma + <^{ik_l}$. We should note that the integrand on the left-hand side has a singular point at the origin. The path of the contour integration is a unit circle at the center γ'/γ in the complex plane, which is parameterized by k_l. Thus, we can evaluate the value of $\Delta\phi_l$ using the residue theorem.

In the trivial phase, i.e., $\gamma'/\gamma \leqslant 1$, $\Delta\phi_l = 0$ because the contour does not enclose the origin. In the nontrivial phase, i.e., $\gamma'/\gamma > 1$, however, $\Delta\phi_l = 2\pi$ because the contour encloses the origin. Therefore, the Zak phase in the 2D SSH model is given as Eq. (6).

APPENDIX B: DERIVATION OF EQUATIONS (8) AND (9)

The charge polarization can be related to the parity of the wave functions. In order to show the relation, let us define the sewing matrix ω, which is in the form of the space-inversion operator Π for the formulation of the Zak phase for a multiband system. Here, Π is an operator that inverts position as $\Pi u(\boldsymbol{k}) = u(-\boldsymbol{k})$. The sewing matrix ω is define as

$$\omega_{ij}(\boldsymbol{k}) := \langle u_i(-\boldsymbol{k})|\Pi|u_j(\boldsymbol{k})\rangle\,, \tag{B1}$$

where i, j are band indexes. In addition, we define the Berry connection matrix as $\boldsymbol{a}_{ij}(\boldsymbol{k}) = -i\,\langle u_i(\boldsymbol{k})|\nabla_{\boldsymbol{k}}|u_j(\boldsymbol{k})\rangle$. By using this matrix, Eq. (7) can be rewritten as

$$P_l = \sum_{j=1}^{occ.}\int_{-\pi}^{\pi}\frac{dk_l}{2\pi}a_{jj}(k_l) \;= \frac{1}{2\pi}\int_{-\pi}^{\pi} dk_l\ \mathrm{Tr}[\boldsymbol{a}_{ij}(k_l)]. \tag{B2}$$

In the presence of space-inversion symmetry, the integrand of Eq. (B2) can be rewritten as [73,74]

$$\mathrm{Tr}[\boldsymbol{a}_{ij}(\boldsymbol{k})] = \mathrm{Tr}[\boldsymbol{a}_{ij}(-\boldsymbol{k})] + i\mathrm{Tr}[\omega_{ij}^{\dagger}(\boldsymbol{k})\nabla_{\boldsymbol{k}}\omega_{ij}(\boldsymbol{k})].$$

Therefore, charge polarization is expressed as

$$\begin{aligned}P_l &= \frac{1}{2\pi}\int_{-\pi}^{\pi} dk_l\left\{\mathrm{Tr}[\boldsymbol{a}(-\boldsymbol{k})] + i\mathrm{Tr}\left[\omega^{\dagger}(\boldsymbol{k})\frac{\partial}{\partial k_l}\omega(\boldsymbol{k})\right]\right\} \\ &= -P_l + q_l^j.\end{aligned}$$

Here, q_l^j is the right hand of the integral element. Using the unitarity of $\omega(\boldsymbol{k})$, the integrand of q_x^j can be rewritten as $\mathrm{Tr}[\omega^\dagger(\boldsymbol{k})\nabla_k\omega(\boldsymbol{k})] = \nabla_k \ln\{\det[\omega(\boldsymbol{k})]\}$. Thus, we obtain

$$q_x^j = -\frac{i}{2\pi}\int_{-\pi}^{\pi} dk_l \frac{d\ln\{\det[\omega(k_x,0)]\}}{dk_l} = -\frac{i}{\pi}\ln\left\{\frac{\det[\omega(\pi,0)]}{\det[\omega(0,0)]}\right\}. \tag{B3}$$

Since the eigenvalue of the space-inversion operator Π is ± 1, $\det[\omega(\boldsymbol{k})]$ is given as

$$\det[\omega(\boldsymbol{k})] = \prod_{j\in occ.} \zeta_j(\boldsymbol{k}), \tag{B4}$$

where $\zeta_j(\boldsymbol{k})$ are the parities of the wave function in the jth energy band at $\boldsymbol{k}$. Substituting Eq. (B4) into Eq. (B3) leads to

$$\ln(e^{i\pi q_x^j}) = \ln\left\{\prod_{j\in occ.}\frac{\zeta_j(\pi,0)}{\zeta_j(0,0)}\right\},$$
$$(-1)^{q_x^j} = \prod_{j\in occ.}\frac{\zeta_j(\mathrm{X})}{\zeta_j(\Gamma)}. \tag{B5}$$

Similarly, the y component is also obtained by replacing X with Y. Thus, q_l^j is topologically invariant, which gives either 0 or 1.

[1] A. Bansil, H. Lin, and T. Das, Rev. Mod. Phys. **88**, 021004 (2016).
[2] M. Z. Hasan and C. L. Kane, Rev. Mod. Phys. **82**, 3045 (2010).
[3] X.-L. Qi and S.-C. Zhang, Rev. Mod. Phys. **83**, 1057 (2011).
[4] C. L. Kane and E. J. Mele, Phys. Rev. Lett. **95**, 226801 (2005).
[5] B. A. Bernevig, T. L. Hughes, and S.-C. Zhang, Science **314**, 1757 (2006).
[6] L. Fu, C. L. Kane, and E. J. Mele, Phys. Rev. Lett. **98**, 106803 (2007).
[7] D. Hsieh, D. Qian, L. Wray, Y. Xia, Y. S. Hor, R. J. Cava, and M. Z. Hasan, Nature (London) **452**, 970 (2008).
[8] Y. L. Chen, J. G. Analytis, J.-H. Chu, Z. K. Liu, S.-K. Mo, X. L. Qi, H. J. Zhang, D. H. Lu, X. Dai, Z. Fang, S. C. Zhang, I. R. Fisher, Z. Hussain, and Z.-X. Shen, Science **325**, 178 (2009).
[9] C.-Z. Chang, J. Zhang, X. Feng, J. Shen, Z. Zhang, M. Guo, K. Li, Y. Ou, P. Wei, L.-L. Wang, Z.-Q. Ji, Y. Feng, S. Ji, X. Chen, J. Jia, X. Dai, Z. Fang, S.-C. Zhang, K. He, Y. Wang, L. Lu, X.-C. Ma, and Q.-K. Xue, Science **340**, 167 (2013).
[10] Y. Ando, J. Phys. Soc. Jpn. **82**, 102001 (2013).
[11] M. Sato and S. Fujimoto, J. Phys. Soc. Jpn. **85**, 072001 (2016).
[12] L. Fu, Phys. Rev. Lett. **106**, 106802 (2011).
[13] Y. Tanaka, Z. Ren, T. Sato, K. Nakayama, S. Souma, T. Takahashi, K. Segawa, and Y. Ando, Nat. Phys. **8**, 800 (2012).
[14] P. Dziawa, B. J. Kowalski, K. Dybko, R. Buczko, A. Szczerbakow, M. Szot, E. Łusakowska, T. Balasubramanian, B. M. Wojek, M. H. Berntsen, O. Tjernberg, and T. Story, Nat. Mater. **11**, 1023 (2012).
[15] Y. Ando and L. Fu, Annu. Rev. Condens. Matter Phys. **6**, 361 (2015).
[16] X. Wan, A. M. Turner, A. Vishwanath, and S. Y. Savrasov, Phys. Rev. B **83**, 205101 (2011).
[17] A. A. Burkov and L. Balents, Phys. Rev. Lett. **107**, 127205 (2011).
[18] S. Borisenko, Q. Gibson, D. Evtushinsky, V. Zabolotnyy, B. Büchner, and R. J. Cava, Phys. Rev. Lett. **113**, 027603 (2014).
[19] Q.-F. Liang, J. Zhou, R. Yu, Z. Wang, and H. Weng, Phys. Rev. B **93**, 085427 (2016).
[20] H. Watanabe, H. C. Po, M. P. Zaletel, and A. Vishwanath, Phys. Rev. Lett. **117**, 096404 (2016).
[21] S. Kobayashi, Y. Yanase, and M. Sato, Phys. Rev. B **94**, 134512 (2016).
[22] B.-J. Yang, T. A. Bojesen, T. Morimoto, and A. Furusaki, Phys. Rev. B **95**, 075135 (2017).
[23] F. Liu and K. Wakabayashi, Jpn. J. Appl. Phys. **58**, SDDD01 (2019).
[24] F. Liu and K. Wakabayashi, Phys. Rev. Lett. **118**, 076803 (2017).
[25] J. Zak, Phys. Rev. Lett. **62**, 2747 (1989).
[26] R. D. King-Smith and D. Vanderbilt, Phys. Rev. B **47**, 1651 (1993).
[27] R. Resta, Rev. Mod. Phys. **66**, 899 (1994).
[28] Y. Zhou, K. M. Rabe, and D. Vanderbilt, Phys. Rev. B **92**, 041102(R) (2015).
[29] M. Hirayama, S. Matsuishi, H. Hosono, and S. Murakami, Phys. Rev. X **8**, 031067 (2018).
[30] H. Huang, K.-H. Jin, S. Zhang, and F. Liu, Nano Lett. **18**, 1972 (2018).
[31] F. Liu, M. Yamamoto, and K. Wakabayashi, J. Phys. Soc. Jpn. **86**, 123707 (2017).
[32] T. Kameda, F. Liu, S. Dutta, and K. Wakabayashi, Phys. Rev. B **99**, 075426 (2019).
[33] W. A. Benalcazar, B. A. Bernevig, and T. L. Hughes, Science **357**, 61 (2017).
[34] W. A. Benalcazar, B. A. Bernevig, and T. L. Hughes, Phys. Rev. B **96**, 245115 (2017).
[35] Z. Song, Z. Fang, and C. Fang, Phys. Rev. Lett. **119**, 246402 (2017).
[36] T. Fukui and Y. Hatsugai, Phys. Rev. B **98**, 035147 (2018).
[37] Z. Wang, B. J. Wieder, J. Li, B. Yan, and B. A. Bernevig, arXiv:1806.11116.
[38] M. Ezawa, Phys. Rev. Lett. **120**, 026801 (2018).
[39] F. Liu, H.-Y. Deng, and K. Wakabayashi, Phys. Rev. Lett. **122**, 086804 (2019).
[40] A. Yoshida, Y. Ohtaki, R. Ohtaki, and T. Fukui, arXiv:1904.05007.
[41] F. Liu, H.-Y. Deng, and K. Wakabayashi, Phys. Rev. B **97**, 035442 (2018).
[42] M. Xiao, Z. Q. Zhang, and C. T. Chan, Phys. Rev. X **4**, 021017 (2014).
[43] B.-Y. Xie, H.-F. Wang, H.-X. Wang, X.-Y. Zhu, J.-H. Jiang, M.-H. Lu, and Y.-F. Chen, Phys. Rev. B **98**, 205147 (2018).
[44] X.-D. Chen, W.-M. Deng, F.-L. Shi, F.-L. Zhao, M. Chen, and J.-W. Dong, Phys. Rev. Lett. **122**, 233902 (2019).
[45] Y. Ota, F. Liu, R. Katsumi, K. Watanabe, K. Wakabayashi, Y. Arakawa, and S. Iwamoto, Optica **6**, 786 (2019).
[46] Y. Liu, C.-S. Lian, Y. Li, Y. Xu, and W. Duan, Phys. Rev. Lett. **119**, 255901 (2017).

[47] X. Zhang, Z.-K. Lin, H.-X. Wang, Z. Xiong, Y. Tian, M.-H. Lu, Y.-F. Chen, and J.-H. Jiang, arXiv:1811.05514.
[48] Z. Zhang, M. Rosendo López, Y. Cheng, X. Liu, and J. Christensen, Phys. Rev. Lett. **122**, 195501 (2019).
[49] L.-Y. Zheng, V. Achilleos, O. Richoux, G. Theocharis, and V. Pagneux, arXiv:1903.11961.
[50] S. Liu, W. Gao, Q. Zhang, S. Ma, L. Zhang, C. Liu, Y. Xiang, T. Cui, and S. Zhang, Research **2019**, 8609875 (2019).
[51] S. Imhof, C. Berger, F. Bayer, J. Brehm, L. W. Molenkamp, T. Kiessling, F. Schindler, C. H. Lee, M. Greiter, T. Neupert, and R. Thomale, Nat. Phys. **14**, 925 (2018).
[52] W. P. Su, J. R. Schrieffer, and A. J. Heeger, Phys. Rev. B **22**, 2099 (1980).
[53] A. J. Heeger, S. Kivelson, J. R. Schrieffer, and W. P. Su, Rev. Mod. Phys. **60**, 781 (1988).
[54] W. Shockley, Phys. Rev. **56**, 317 (1939).
[55] S. S. Pershoguba and V. M. Yakovenko, Phys. Rev. B **86**, 075304 (2012).
[56] S. Sayed, Ph.D. thesis, Purdue University, 2018.
[57] M. Fujita, K. Wakabayashi, K. Nakada, and K. Kusakabe, J. Phys. Soc. Jpn. **65**, 1920 (1996).
[58] K. Nakada, M. Fujita, G. Dresselhaus, and M. S. Dresselhaus, Phys. Rev. B **54**, 17954 (1996).
[59] K. Wakabayashi, M. Fujita, H. Ajiki, and M. Sigrist, Phys. Rev. B **59**, 8271 (1999).
[60] P. Delplace, D. Ullmo, and G. Montambaux, Phys. Rev. B **84**, 195452 (2011).
[61] D. J. Rizzo, G. Veber, T. Cao, C. Bronner, T. Chen, F. Zhao, H. Rodriguez, S. G. Louie, M. F. Crommie, and F. R. Fischer, Nature (London) **560**, 204 (2018).
[62] O. Gröning, S. Wang, X. Yao, C. A. Pignedoli, G. B. Barin, C. Daniels, A. Cupo, V. Meunier, X. Feng, A. Narita, K. Müllen, P. Ruffieux, and R. Fasel, Nature (London) **560**, 209 (2018).
[63] K. Wakabayashi, Y. Takane, and M. Sigrist, Phys. Rev. Lett. **99**, 036601 (2007).
[64] K. Wakabayashi, Y. Takane, M. Yamamoto, and M. Sigrist, New J. Phys. **11**, 095016 (2009).
[65] K. Wakabayashi, Y. Takane, M. Yamamoto, and M. Sigrist, Carbon **47**, 124 (2009).
[66] J. Baringhaus, M. Ruan, F. Edler, A. Tejeda, M. Sicot, A. Taleb-Ibrahimi, A.-P. Li, Z. Jiang, E. H. Conrad, C. Berger, C. Tegenkamp, and W. A. d. Heer, Nature (London) **506**, 349 (2014).
[67] K. Wakabayashi, K.-i. Sasaki, T. Nakanishi, and T. Enoki, Sci. Technol. Adv. Mater. **11**, 054504 (2010).
[68] K. Wakabayashi and S. Dutta, Solid State Commun. **152**, 1420 (2012).
[69] C. Fang, M. J. Gilbert, and B. A. Bernevig, Phys. Rev. B **86**, 115112 (2012).
[70] J. Nakabayashi, D. Yamamoto, and S. Kurihara, Phys. Rev. Lett. **102**, 066803 (2009).
[71] H.-Y. Deng and K. Wakabayashi, Phys. Rev. B **90**, 045402 (2014).
[72] C. W. Duncan, P. Öhberg, and M. Valiente, Phys. Rev. B **97**, 195439 (2018).
[73] L. Fu and C. L. Kane, Phys. Rev. B **76**, 045302 (2007).
[74] B. A. Bernevig and T. L. Hughes, *Topological Insulators and Topological Superconductors* (Princeton University Press, Princeton, NJ, 2013).